

# Isogeometric finite element analysis of functionally graded plates using a refined plate theory

H. Nguyen-Xuan<sup>1,2\*</sup>, Loc V. Tran<sup>3</sup>, Chien H. Thai<sup>3</sup>, S. Kulasegaram<sup>1</sup>, S.P.A. Bordas<sup>1</sup>

<sup>1</sup>Institute of Mechanics and Advanced Materials, School of Engineering, Cardiff University, Queen's Buildings, The Parade, Cardiff CF24 3AA, UK

<sup>2</sup>Department of Mechanics, Faculty of Mathematics & Computer Science, University of Science Ho Chi Minh City, Vietnam

<sup>3</sup>Division of Computational Mechanics, Ton Duc Thang University Ho Chi Minh City, Vietnam

## Abstract

We propose in this paper a novel inverse tangent transverse shear deformation formulation for functionally graded material (FGM) plates. The isogeometric finite element analysis (IGA) of static, free vibration and buckling problems of FGM plates is then addressed using a refined plate theory (RPT). The RPT enables us to describe the non-linear distribution of shear stresses through the plate thickness without any requirement of shear correction factors (SCF). IGA utilizes basis functions, namely B-splines or non-uniform rational B-splines (NURBS), which achieve easily the smoothness of any arbitrary order. It hence satisfies the  $C^1$  requirement of the RPT model. The present method approximates the displacement field of four degrees of freedom per each control point and retains the computational efficiency while ensuring the high accuracy in solution.

**Keywords:** plate structures, functionally graded material (FGM), isogeometric analysis (IGA), refined plate theory (RPT).

## 1. Introduction

FGM—a mixture of two distinct material phases: ceramic and metal, e.g. Figure 1, are very well capable of reducing thermal stresses, resisting high temperature environment and corrosion coatings. FG plates are therefore suitable for applications in aerospace structures, nuclear plants and semiconductor technologies. They have hence been received great attention by many researchers.

---

\* Corresponding author. *Email address:* [nxhung@hcmus.edu.vn](mailto:nxhung@hcmus.edu.vn) (H. Nguyen-Xuan)

Besides the extensive application of FG plates in engineering structures, a lot of plate theories have been developed to analyze the thermo-mechanical behavior of such structures. The Classical Plate Theory (CPT) relied on the Kirchoff-Love assumptions merely to provide acceptable results for the thin plate. The First Order Shear Deformation Theory (FSDT) based on Reissner [1] and Mindlin [2], which takes into account the shear effect, was therefore developed. In FSDT-based finite element models, it is necessary to use some improved techniques such as reduced integration (RI) [3], mixed interpolation of tensorial components (MITC) [4], Mindlin-type plate element with improved transverse shear(MIN) [5], discrete shear gap (DSG) [6-8] elements, etc, to overcome the shear locking phenomenon. In addition, with the linear in-plane displacement assumption through plate thickness, shear strain/stress obtained from FSDT distributes inaccurately and does not satisfy the traction free boundary conditions at the plate surfaces. The shear correction factors (SCF) are hence required to rectify the unrealistic shear strain energy part. The values of SCF are quite dispersed through each problem and may be difficult to determine [9]. To ensure the curved distribution of shear stress, various kinds of Higher-Order Shear Deformable Theory (HSDT), which includes higher-order terms in the approximation of the displacement field, have then been devised such as Third-Order Shear Deformation Theory (TSDT) [10-14], trigonometric shear deformation theory [15-19], exponential shear deformation theory [20-22], refined plate theory (RPT) based on two unknown functions of transverse deflection [23,24] and so on. The two variable RPT model was first proposed by Shimpi [25] using only two unknown variables for the isotropic plate and then extended for the orthotropic plate [26,27]. It is worth mentioning that the HSDT models provide better results and yield more accurate and stable solutions (e.g. inter-laminar stresses and displacements) [28,29] than the FSDT ones without requirement the SCF. However, the HSDT requires the  $C^1$ -continuity of generalized displacement field leading to the second-order derivative of the stiffness formulation and it causes the obstacles in the standard finite element formulations. Several  $C^0$  continuous elements [30-34] were proposed or Hermite interpolation function with the  $C^1$ -continuity was added for just specific approximation of transverse displacement [10]. It may produce extra unknown variables including derivative of deflection  $w_{,x}$ ,  $w_{,y}$ ,  $w_{,xy}$  [35] leading to increase in the computational cost. In this paper, we show that  $C^1$ -continuous elements will be easily achieved by IGA without any additional variables.

Isogeometric approach (IGA) has been recently proposed by Hughes et al. [36] to closely link the gap between Computer Aided Design (CAD) and Finite Element Analysis (FEA). The basic idea is that the IGA uses the same non-uniform rational B-Spline (NURBS) functions in describing the exact geometry of problem and constructing finite approximation for analysis. It is well known that NURBS

functions provide a flexible way to make refinement, de-refinement, and degree elevation [37]. They enable us to easily achieve the smoothness of arbitrary continuity order in comparison with the traditional FEM. Hence, IGA naturally verifies the  $C^1$ -continuity of plates based on the HSDT assumption, which is interested in this study. The IGA has been well known and widely applied to various practical problems [38-44] and so on.

In this paper, a novel inverse tangent transverse shear deformation plate theory with four parameters of displacement field are proposed to study the behavior of the FGM plates based on NURBS-based IGA approximation. The RPTs are independent on SCF and free from shear locking. The material property changing continuously through plate thickness is homogenized by the rule of mixture and the Mori-Tanaka homogenization technique. IGA utilizes the NURBS functions which achieve easily the smoothness with arbitrary continuous order. It helps the present method to naturally satisfy the  $C^1$  continuous requirement of this plate theory. Numerous numerical examples are provided to illustrate the effectiveness of the present formulation in comparison with other published models.

The paper is outlined as follows. Next section introduces the novel RPT for FGM plates. In section 3, the formulation of plate theory based on IGA is described. The numerical results and discussions are provided in section 4. Finally, this article is closed with some concluding remarks.

## 2. The novel refined plate theory for FGM plates

### 2.1. Functionally graded material

Functionally graded material is a composite material which is created by mixing two distinct material phases which are often ceramic at the top and metal at the bottom. In this paper, two homogenous models have been used to estimate the effective properties of the FGM including the rule of mixture and the Mori-Tanaka technique. The volume fraction of the ceramic and metal phase is assumed continuous variation through thickness as the following exponent function [10]

$$V_c(z) = \left( \frac{1}{2} + \frac{z}{h} \right)^n, \quad V_m = 1 - V_c \quad (1)$$

where subscripts  $m$  and  $c$  refer to the metal and ceramic constituents, respectively. Eq. (1) denotes that the volume fraction varies through the thickness based on the power index  $n$ .

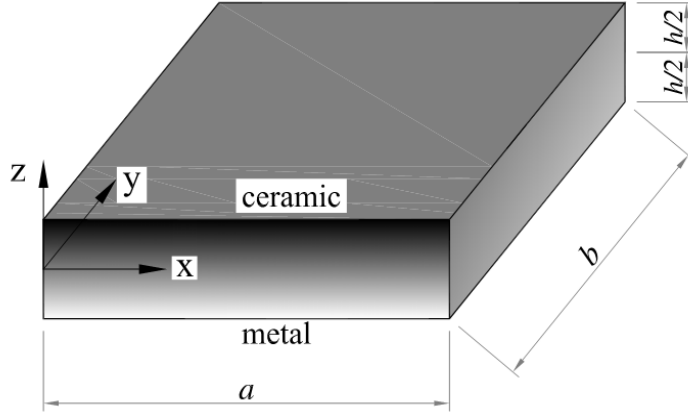


Figure 1: The functionally graded plate model.

Then, the effective properties of material according to the rule of mixture [10] are given by

$$P_e = P_c V_c(z) + P_m V_m(z) \quad (2)$$

where  $P_c, P_m$  denote the individual material's properties of the ceramic and the metal, respectively including the Young's modulus  $E$ , Poisson's ratio  $\nu$ , density  $\rho$ .

However, the rule of mixture does not consider the interactions among the constituents [46,47]. So, the Mori-Tanaka technique [45] is then developed to take into account these interactions with the effective bulk and shear modulus defined from following relations:

$$\begin{aligned} \frac{K_e - K_m}{K_c - K_m} &= \frac{V_c}{1 + V_m \frac{K_c - K_m}{K_m + 4/3 \mu_m}} \\ \frac{\mu_e - \mu_m}{\mu_c - \mu_m} &= \frac{V_c}{1 + V_m \frac{\mu_c - \mu_m}{\mu_m + f_1}} \end{aligned} \quad (3)$$

where  $f_1 = \frac{\mu_m(9K_m + 8\mu_m)}{6(K_m + 2\mu_m)}$ . Then, the effective values of Young's modulus  $E_e$  and Poisson's ratio  $\nu_e$

are given by:

$$E_e = \frac{9K_e \mu_e}{3K_e + \mu_e}, \quad \nu_e = \frac{3K_e - 2\mu_e}{2(3K_e + \mu_e)} \quad (4)$$

Figure 2 illustrates the comparison of the effective Young's modulus of Al/ZrO<sub>2</sub> FGM plate calculated by the rule of mixture and the Mori-Tanaka scheme via the power index  $n$ . It is noted that

with homogeneous materials, two models give the same values, however as material becomes inhomogeneous, the effective property through the thickness of the former is higher than the latter one.

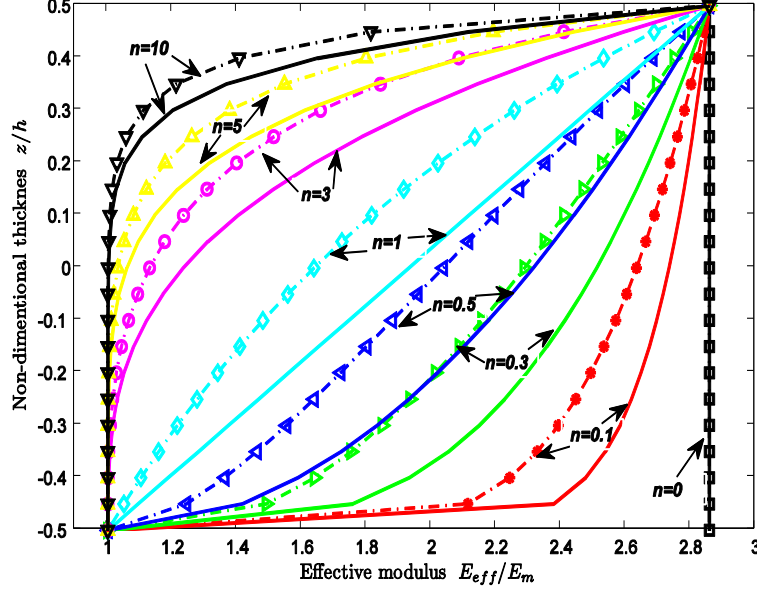


Figure 2. The effective modulus of Al/ZrO<sub>2</sub> FGM plate computed by the rule of mixture (in solid line) and the Mori-Tanaka (in dash dot line).

## 2.2. The novel inverse tangent transverse shear deformation plate theories

A general displacement field based on refined plate theory according to Shimpi [25] is defined as follows

$$\begin{aligned} u(x, y, z) &= u_0 - zw_{b,x} + g(z)w_{s,x} \\ v(x, y, z) &= v_0 - zw_{b,y} + g(z)w_{s,y} \quad , \quad \left( \frac{-h}{2} \leq z \leq \frac{h}{2} \right) \\ w(x, y) &= w_b + w_s \end{aligned} \quad (5)$$

where  $u_0, v_0$  are the membrane displacements along the  $x, y$  axis respectively and  $w_b, w_s$  are the bending and shear components of deflection and the function  $g(z) = f(z) - z$  is used to describe the distribution of the transverse shear strains and stresses through the plate thickness. The function  $f(z)$  is chosen to satisfy the tangential zero value at  $z = \pm h/2$ . It means that traction-free boundary condition at the top and bottom plate surfaces is automatically satisfied. In this study, beyond some existing shape functions [10,20,21,48], we propose two inverse tangent formulations for  $f(z)$  as listed in Table 1.

Table 1: The various forms of shape function.

Model	$f(z)$	$f'(z)$
Reddy [10]	$z - \frac{4}{3}z^3 / h^2$	$1 - 4z^2 / h^2$
Karama [20]	$ze^{-2(z/h)^2}$	$(1 - \frac{4}{h^2}z^2)e^{-2(z/h)^2}$
Arya [21]	$\sin(\frac{\pi}{h}z)$	$\frac{\pi}{h}\cos(\frac{\pi}{h}z)$
Nguyen-Xuan [48]	$\frac{7}{8}z - \frac{2}{h^2}z^3 + \frac{2}{h^4}z^5$	$\frac{7}{8} - \frac{6}{h^2}z^2 + \frac{10}{h^4}z^4$
Proposed model 1	$h\arctan(\frac{2}{h}z) - z$	$(1 - (\frac{2}{h}z)^2) / (1 + (\frac{2}{h}z)^2)$
Proposed model 2	$\arctan(\sin(\frac{\pi}{h}z))$	$\frac{\pi}{h}\cos(\frac{\pi}{h}z) / (1 + \sin^2(\frac{\pi}{h}z))$

The relationship between strains and displacements is described by

$$\boldsymbol{\varepsilon} = [\varepsilon_{xx} \ \varepsilon_{yy} \ \gamma_{xy}]^T = \boldsymbol{\varepsilon}_0 + z\boldsymbol{\kappa}_b + g(z)\boldsymbol{\kappa}_s \quad (6)$$

$$\boldsymbol{\gamma} = [\gamma_{xz} \ \gamma_{yz}]^T = f'(z)\boldsymbol{\varepsilon}_s$$

where

$$\boldsymbol{\varepsilon}_0 = \begin{bmatrix} u_{0,x} \\ v_{0,y} \\ u_{0,y} + v_{0,x} \end{bmatrix}, \boldsymbol{\kappa}_b = - \begin{bmatrix} w_{b,xx} \\ w_{b,yy} \\ 2w_{b,xy} \end{bmatrix}, \boldsymbol{\kappa}_s = \begin{bmatrix} w_{s,xx} \\ w_{s,yy} \\ 2w_{s,xy} \end{bmatrix}, \boldsymbol{\varepsilon}_s = \begin{bmatrix} w_{s,x} \\ w_{s,y} \end{bmatrix} \quad (7)$$

A weak form of the static model for the plates under transverse loading  $q_0$  can be briefly expressed as:

$$\int_{\Omega} \delta \boldsymbol{\varepsilon}^T \mathbf{D}^b \boldsymbol{\varepsilon} d\Omega + \int_{\Omega} \delta \boldsymbol{\gamma}^T \mathbf{D}^s \boldsymbol{\gamma} d\Omega = \int_{\Omega} \delta w q_0 d\Omega \quad (8)$$

where

$$\mathbf{D}^b = \begin{bmatrix} \mathbf{A} & \mathbf{B} & \mathbf{E} \\ \mathbf{B} & \mathbf{D} & \mathbf{F} \\ \mathbf{E} & \mathbf{F} & \mathbf{H} \end{bmatrix} \quad (9)$$

$$A_{ij}, B_{ij}, D_{ij}, E_{ij}, F_{ij}, H_{ij} = \int_{-h/2}^{h/2} (1, z, z^2, g(z), zg(z), g^2(z)) Q_{ij} dz$$

$$D_{ij}^s = \int_{-h/2}^{h/2} [f'(z)]^2 G_{ij} dz$$

and the material matrices are given as

$$\mathbf{Q} = \frac{E_e}{1-\nu_e^2} \begin{bmatrix} 1 & \nu_e & 0 \\ \nu_e & 1 & 0 \\ 0 & 0 & (1-\nu_e)/2 \end{bmatrix} \quad (10)$$

$$\mathbf{G} = \frac{E_e}{2(1+\nu_e)} \begin{bmatrix} 1 & 0 \\ 0 & 1 \end{bmatrix}$$

For the free vibration analysis of the plates, weak form can be derived from the following dynamic equation

$$\int_{\Omega} \delta \boldsymbol{\varepsilon}^T \mathbf{D}^b \boldsymbol{\varepsilon} d\Omega + \int_{\Omega} \delta \boldsymbol{\gamma}^T \mathbf{D}^s \boldsymbol{\gamma} d\Omega = \int_{\Omega} \delta \tilde{\mathbf{u}}^T \mathbf{m} \ddot{\mathbf{u}} d\Omega \quad (11)$$

where  $\mathbf{m}$  - the mass matrix is calculated according to the consistent form

$$\mathbf{m} = \begin{bmatrix} \mathbf{I}_0 & 0 & 0 \\ 0 & \mathbf{I}_0 & 0 \\ 0 & 0 & \mathbf{I}_0 \end{bmatrix} \quad \text{where } \mathbf{I}_0 = \begin{bmatrix} I_1 & I_2 & I_4 \\ I_2 & I_3 & I_5 \\ I_4 & I_5 & I_6 \end{bmatrix} \quad (12)$$

$$(I_1, I_2, I_3, I_4, I_5, I_6) = \int_{-h/2}^{h/2} \rho(z) (1, z, z^2, zg(z), zg(z), g^2(z)) dz. \quad (13)$$

and

$$\tilde{\mathbf{u}} = \begin{Bmatrix} \mathbf{u}_1 \\ \mathbf{u}_2 \\ \mathbf{u}_3 \end{Bmatrix}, \quad \mathbf{u}_1 = \begin{Bmatrix} u_0 \\ -w_{b,x} \\ w_{s,x} \end{Bmatrix}; \quad \mathbf{u}_2 = \begin{Bmatrix} v_0 \\ -w_{b,y} \\ w_{s,y} \end{Bmatrix}; \quad \mathbf{u}_3 = \begin{Bmatrix} w \\ 0 \\ 0 \end{Bmatrix} \quad (14)$$

For the buckling analysis, a weak form of the plate under the in-plane forces can be expressed as:

$$\int_{\Omega} \delta \boldsymbol{\varepsilon}^T \mathbf{D}^b \boldsymbol{\varepsilon} d\Omega + \int_{\Omega} \delta \boldsymbol{\gamma}^T \mathbf{D}^s \boldsymbol{\gamma} d\Omega + \int_{\Omega} \nabla^T \delta w \mathbf{N}_0 \nabla w d\Omega = 0 \quad (15)$$

where  $\nabla^T = [\partial / \partial x \quad \partial / \partial y]^T$  is the gradient operator and  $\mathbf{N}_0 = \begin{bmatrix} N_x^0 & N_{xy}^0 \\ N_{xy}^0 & N_y^0 \end{bmatrix}$  is a matrix related to the pre-

buckling loads.

### 3. The FGM plate formulation based on NURBS basis functions

#### 3.1. A brief of NURBS functions



A knot vector  $\boldsymbol{\xi} = \{\xi_1, \xi_2, \dots, \xi_{n+p+1}\}$  is defined as a sequence of knot value  $\xi_i \in R$ ,  $i = 1, \dots, n+p$ . If the

first and the last knots are repeated  $p+1$  times, the knot vector is called open knot. A B-spline basis function is  $C^\infty$  continuous inside a knot span and  $C^{p-1}$  continuous at a single knot. Thus, as  $p \geq 2$  the present approach always satisfies  $C^1$ -requirement in approximate formulations of RPT.

The B-spline basis functions  $N_{i,p}(\xi)$  are defined by the following recursion formula

$$N_{i,p}(\xi) = \frac{\xi - \xi_i}{\xi_{i+p} - \xi_i} N_{i,p-1}(\xi) + \frac{\xi_{i+p+1} - \xi}{\xi_{i+p+1} - \xi_{i+1}} N_{i+1,p-1}(\xi)$$

$$\text{as } p = 0, N_{i,0}(\xi) = \begin{cases} 1 & \text{if } \xi_i < \xi < \xi_{i+1} \\ 0 & \text{otherwise} \end{cases}$$
(16)

By the tensor product of basis functions in two parametric dimensions  $\xi$  and  $\eta$  with two knot vectors  $\Xi = \{\xi_1, \xi_2, \dots, \xi_{n+p+1}\}$  and  $\mathbf{H} = \{\eta_1, \eta_2, \dots, \eta_{m+q+1}\}$ , the two-dimensional B-spline basis functions are obtained

$$N_A(\xi, \eta) = N_{i,p}(\xi) M_{j,q}(\eta)$$
(17)

Figure 3 illustrates the set of one-dimensional and two-dimensional B-spline basis functions according to open uniform knot vector  $\Xi = \{0, 0, 0, 0, \frac{1}{2}, 1, 1, 1, 1\}$ .

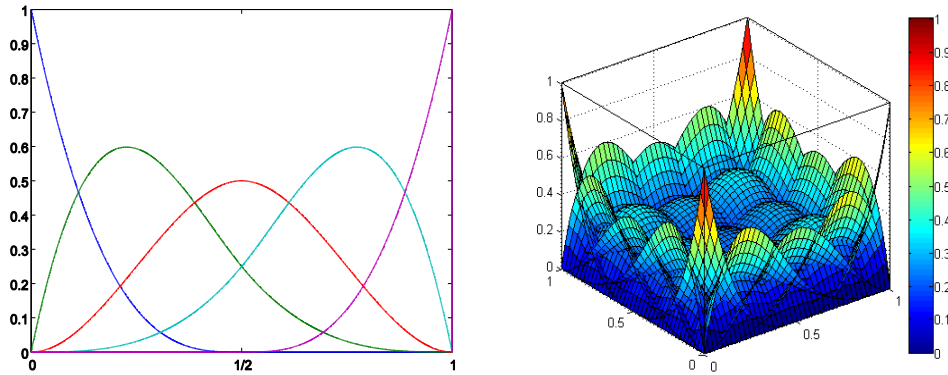


Figure 3. 1D and 2D B-spline basis functions.

To present exactly some curved geometry (e.g. circles, cylinders, spheres, etc.) the non-uniform rational B-splines (NURBS) functions are used. Be different from B-spline, each control point of NURBS has additional value called an individual weight  $w_A$  [36]. Then the NURBS functions can be expressed as



$$R_A(\xi, \eta) = \frac{N_A w_A}{\sum_A^{m \times n} N_A(\xi, \eta) w_A} \quad (18)$$

It can be noted that B-spline function is only the special case of the NURBS function when the individual weight of control point is constant.

### 3.2. A novel RPT formulation based on NURBS approximation

Using the NURBS basis functions above, the displacement field  $\mathbf{u}$  of the plate is approximated as

$$\mathbf{u}^h(\xi, \eta) = \sum_A^{m \times n} R_A(\xi, \eta) \mathbf{q}_A \quad (19)$$

where  $\mathbf{q}_A = [u_{0A} \ v_{0A} \ w_{bA} \ w_{sA}]^T$  is the vector of nodal degrees of freedom associated with the control point A.

Substituting Eq. (19) into Eq. (7), the in-plane and shear strains can be rewritten as:

$$\left[ \boldsymbol{\varepsilon}_0^T \ \boldsymbol{\kappa}_b^T \ \boldsymbol{\kappa}_s^T \ \boldsymbol{\varepsilon}_s^T \right]^T = \sum_{A=1}^{m \times n} \left[ (\mathbf{B}_A^m)^T \ (\mathbf{B}_A^{b1})^T \ (\mathbf{B}_A^{b2})^T \ (\mathbf{B}_A^s)^T \right]^T \mathbf{q}_A \quad (20)$$

in which

$$\mathbf{B}_A^m = \begin{bmatrix} R_{A,x} & 0 & 0 & 0 \\ 0 & R_{A,y} & 0 & 0 \\ R_{A,y} & R_{A,x} & 0 & 0 \end{bmatrix}, \quad \mathbf{B}_A^{b1} = - \begin{bmatrix} 0 & 0 & R_{A,xx} & 0 \\ 0 & 0 & R_{A,yy} & 0 \\ 0 & 0 & 2R_{A,xy} & 0 \end{bmatrix}, \quad (21)$$

$$\mathbf{B}_A^{b2} = \begin{bmatrix} 0 & 0 & 0 & R_{A,xx} \\ 0 & 0 & 0 & R_{A,yy} \\ 0 & 0 & 0 & 2R_{A,xy} \end{bmatrix}, \quad \mathbf{B}_A^s = \begin{bmatrix} 0 & 0 & 0 & R_{A,x} \\ 0 & 0 & 0 & R_{A,y} \end{bmatrix}$$

Substituting Eq. (20) into Eqs.(8), (11) and (15), the formulations of static, free vibration and buckling problem are rewritten in the following form

$$\mathbf{K}\mathbf{q} = \mathbf{F} \quad (22)$$

$$(\mathbf{K} - \omega^2 \mathbf{M})\mathbf{q} = \mathbf{0} \quad (23)$$

$$(\mathbf{K} - \lambda_{cr} \mathbf{K}_g)\mathbf{q} = \mathbf{0} \quad (24)$$

where the global stiffness matrix  $\mathbf{K}$  is given by

$$\mathbf{K} = \int_{\Omega} \begin{Bmatrix} \mathbf{B}^m \\ \mathbf{B}^{b1} \\ \mathbf{B}^{b2} \end{Bmatrix}^T \begin{bmatrix} \mathbf{A} & \mathbf{B} & \mathbf{E} \\ \mathbf{B} & \mathbf{D} & \mathbf{F} \\ \mathbf{E} & \mathbf{F} & \mathbf{H} \end{bmatrix} \begin{Bmatrix} \mathbf{B}^m \\ \mathbf{B}^{b1} \\ \mathbf{B}^{b2} \end{Bmatrix} + \mathbf{B}^{sT} \mathbf{D}^s \mathbf{B}^s d\Omega \quad (25)$$

and the load vector is computed by

$$\mathbf{F} = \int_{\Omega} q_0 \mathbf{R} d\Omega \quad (26)$$

where

$$\mathbf{R} = [0 \quad 0 \quad R_A \quad R_A] \quad (27)$$

the global mass matrix  $\mathbf{M}$  is expressed as

$$\mathbf{M} = \int_{\Omega} \tilde{\mathbf{R}}^T \mathbf{m} \tilde{\mathbf{R}} d\Omega \quad (28)$$

where

$$\tilde{\mathbf{R}} = \begin{Bmatrix} \mathbf{R}_1 \\ \mathbf{R}_2 \\ \mathbf{R}_3 \end{Bmatrix}, \quad \mathbf{R}_1 = \begin{bmatrix} R_A & 0 & 0 & 0 \\ 0 & 0 & -R_{A,x} & 0 \\ 0 & 0 & 0 & R_{A,x} \end{bmatrix}; \quad (29)$$

$$\mathbf{R}_2 = \begin{bmatrix} 0 & R_A & 0 & 0 \\ 0 & 0 & -R_{A,y} & 0 \\ 0 & 0 & 0 & R_{A,y} \end{bmatrix}; \quad \mathbf{R}_3 = \begin{bmatrix} 0 & 0 & R_A & R_A \\ 0 & 0 & 0 & 0 \\ 0 & 0 & 0 & 0 \end{bmatrix}$$

the geometric stiffness matrix is

$$\mathbf{K}_g = \int_{\Omega} (\mathbf{B}^g)^T \mathbf{N}_0 \mathbf{B}^g d\Omega \quad (30)$$

where

$$\mathbf{B}_A^g = \begin{bmatrix} 0 & 0 & R_{A,x} & R_{A,x} \\ 0 & 0 & R_{A,y} & R_{A,y} \end{bmatrix} \quad (31)$$

in which  $\omega, \lambda_{cr} \in R^+$  are the natural frequency and the critical buckling value, respectively.

It is observed from Eq. (25) that the SCF is no longer required in the stiffness formulation. Herein,  $\mathbf{B}_A^{b1}$  and  $\mathbf{B}_A^{b2}$  contain the second-order derivative of the shape function. Hence, it requires  $C^1$ -

continuous element in approximate formulations. It is now interesting to note that our present formulation based on IGA naturally satisfies  $C^1$ -continuity from the theoretical/mechanical viewpoint of FGM plates [43, 29]. In our work, the basis functions are  $C^{p-1}$  continuous. Therefore, as  $p \geq 2$ , the present approach always satisfies  $C^1$ -requirement in approximate formulations based on the proposed RPT.

#### 4. Results and discussions

In this section, the plates with two kinds of shape such as square and circle are modeled. The FGM plates are made from Aluminum/Alumina (Al/Al<sub>2</sub>O<sub>3</sub>) or Aluminum/Zirconia (Al/ZrO<sub>2</sub>) and the properties of which are listed in Table 2. Numerical results are obtained by IGA with full  $(p+1) \times (q+1)$  Gauss points. In addition, two types of boundary condition are applied including:

Simply supported (S):

$$\begin{aligned} v_0 = w_b = w_s = 0 & \quad \text{at } x=0, a \\ u_0 = w_b = w_s = 0 & \quad \text{at } y=0, b \end{aligned} \quad (32)$$

Clamped (C):

$$u_0 = v_0 = w_b = w_s = w_{b,n} = w_{s,n} = 0 \quad (33)$$

The Dirichlet BCs on  $u_0, v_0, w_b$  and  $w_s$  is easily treated as in the standard FEM. However, for the derivatives  $w_{b,n}, w_{s,n}$  the enforcement of Dirichlet BCs can be solved in a simple and effective way [49]. The idea is as follows. The derivatives can be included in a compact form of the normal slope at the boundary:

$$\frac{\partial w}{\partial n} = \lim_{\Delta n \rightarrow 0} \frac{w(n(\mathbf{x}_C) + \Delta n) - w(n(\mathbf{x}_C))}{\Delta n} = 0 \quad (34)$$

As  $w(n(\mathbf{x}_C)) = 0$  according to Eq. (33), Eq. (34) leads to impose the same boundary values, i.e., zero values, on the deflection variable at control points  $\mathbf{x}_A$  which is adjacent to the boundary control points  $\mathbf{x}_C$ . It can be observed that, implementing the essential boundary condition using this method is very simple in IGA compare to other numerical methods.

Table 2: Material properties.

	Al	SiC	ZrO <sub>2</sub> -1	ZrO <sub>2</sub> -2	Al <sub>2</sub> O <sub>3</sub>
$E$ (GPa)	70	427	200	151	380
$\nu$	0.3	0.17	0.3	0.3	0.3
$\rho$ (kg/m <sup>3</sup> )	2707	-	5700	3000	3800

#### 4.1 Convergence study

Let us consider the simply supported Al/SiC square FGM plate shown in Figure 4a, for which properties are given in

Table 2. The plate is subjected to a sinusoidal pressure defined as  $q_0 \sin(\frac{\pi x}{a}) \sin(\frac{\pi y}{a})$  at the top surface.

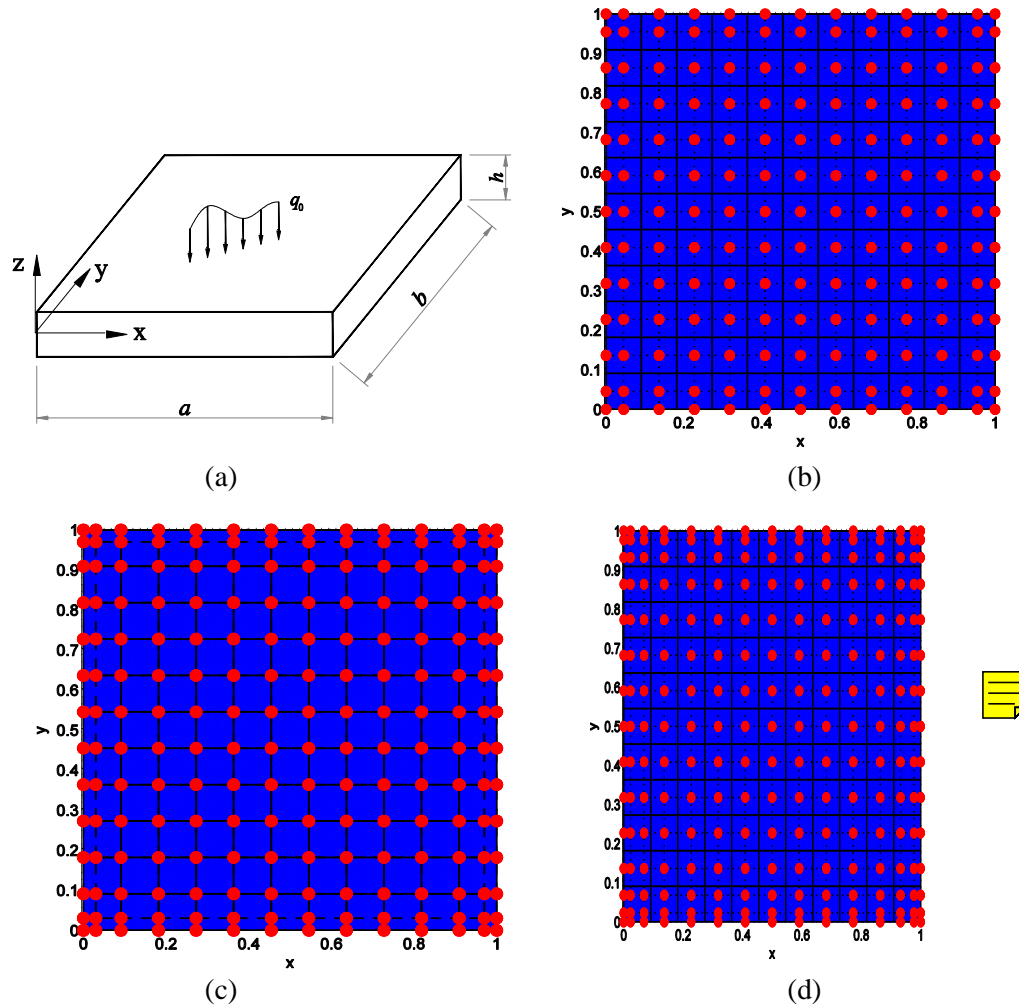


Figure 4. Square plate: (a) The plate geometry; (b), (c), (d): meshing of 11x11 quadratic, cubic and quartic elements, respectively.

A convergent study of transverse displacement by quadratic ( $p = 2$ ) cubic ( $p = 3$ ) and quartic ( $p = 4$ ) elements is depicted in Figure 6 according to  $n = 1$  and 6, respectively. It is observed that, as number of element increases the obtained results converge to exact solutions from 3D deformation model by

Vel and Batra [46]. IGA, moreover, gains the super-convergence with the discrepancy between meshing of  $5 \times 5$  and  $25 \times 25$  around  $0.05\%$  as  $p \geq 3$ . Here, using the RPT with function  $f(z)$  proposed by Reddy [10], the present method, which just uses  $11 \times 11$  cubic NURBS elements shown in Figure 4c, produces an ultra-accurate solution that is very close to the exact solution with very small error around  $0.02\%$ . Therefore, in the next problems, the meshing of  $11 \times 11$  cubic NURBS elements is used.

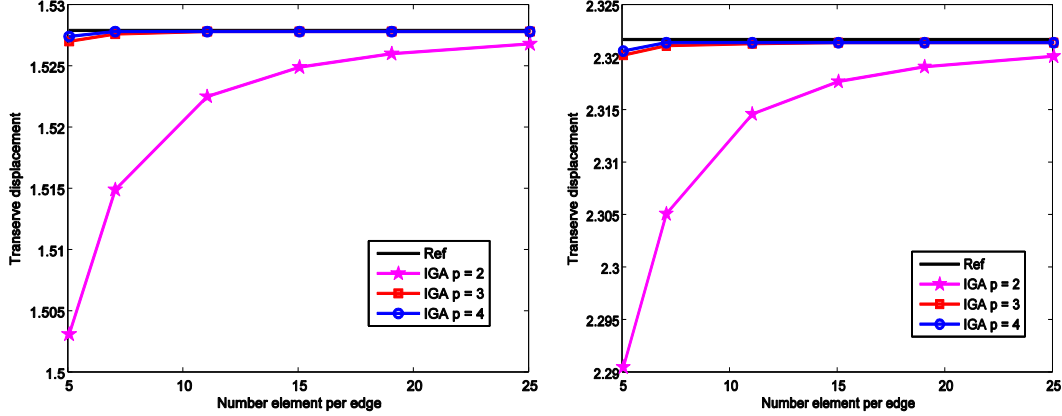


Figure 5. Comparison of present result with analytical solution of Vel and Batra according to power index  $n = 1$  and  $6$ , respectively.

Next, the shear locking phenomenon is investigated for an isotropic plate which is subjected to a uniform transverse load  $q_0$ . Figure 6 reveals the relation between the central deflection and the length to thickness ratio under full simply supported and full clamped conditions. By using various  $f(z)$  functions in [21, 48] and the two proposed models 1 & 2, it is seen that all obtained results are the same for this problem. Those solutions are in good agreement with that using TSDT based on the Mindlin plate model with 5DOFs/node provided in [29] for moderate thick and thick plates. However, as plate becomes very thin ( $a/h > 1000$ ) the obtained results from TSDT with 5DOFs are not asymptotic to that of CPT [51]. It is called shear-locking phenomenon. Herein, with two approximated variables for transverse displacement according to Eq. (5), the shear strains/stresses are obtained independently on the bending component. As a result, the RPT has strong similarity with the CPT and will be free of shear-locking. The present results therefore match well with the thin plate result [51], even at  $a/h = 10^6$ .

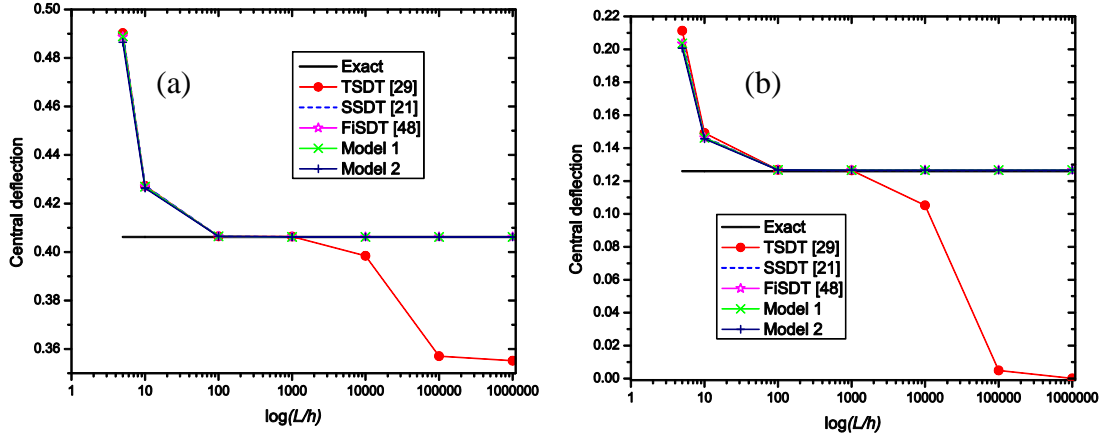


Figure 6. The center deflection via length to thickness ratio under boundary conditions: (a) full support (SSSS), (b) full clamped (CCCC).

#### 4.2 Static analysis

In this example, the Al/Al<sub>2</sub>O<sub>3</sub> FGM plate subjected to a sinusoidal pressure defined as  $q_0 \sin(\frac{\pi x}{a}) \sin(\frac{\pi y}{a})$  is considered. It is noted that the material properties are computed by the rule of mixture based on Eq. (2). Using different functions  $f(z)$  given in Table 1, the results based on RPT including deflection  $\bar{w}$  and axial stress  $\bar{\sigma}_x(\frac{h}{3})$  at plate center are summarized in Table 3. The solutions are in good agreement with that of Zenkour's generalized shear deformation theory [52], and those from Carrera et al. [53,58] using Carrera's unified formulation and Neves et al. [54,55] using sinusoidal shear deformation theory (SSDT) and HSDT models. It is concluded that the quasi 3D models accounting for the thickness stretching effect  $\varepsilon_z \neq 0$  gain the lower transverse displacement and higher axial stress than the 2D plate models which eliminate the stretching effect. However, the discrepancy between two models reduces as the plate becomes thinner. Figure 7 plots the stress distribution through the thickness of thick plate with  $a/h = 4$  and  $n = 1$ . Using RPT models, the axial stress is plotted in the same path while there is a slight difference observed for shear stress distribution. And, all of them satisfy the traction-free boundary conditions at the plate surfaces.

Table 3: The non-dimensional deflection and, axial stress of SSSS Al/Al<sub>2</sub>O<sub>3</sub> square plate under sinusoidal load.

$n$	Model	$\varepsilon_z$	$a/h = 4$		10		100	
			$\bar{w}$	$\bar{\sigma}_x(z = \frac{h}{3})$	$\bar{w}$	$\bar{\sigma}_x(z = \frac{h}{3})$	$\bar{w}$	$\bar{\sigma}_x(z = \frac{h}{3})$
	Ref. [58]	$\neq 0$	0.7171	0.6221	0.5875	1.5064	0.5625	14.969
	CLT	0	0.5623	0.806	0.5623	2.015	0.5623	20.15
	FSDT	0	0.7291	0.806	0.5889	2.015	0.5625	20.15

	GSDT [52]	0	-	-	0.5889	1.4894	-	-
	Ref.[53]	0	0.7289	0.7856	0.589	2.0068	0.5625	20.149
	Ref.[53]	≠0	0.7171	0.6221	0.5875	1.5064	0.5625	14.969
1	SSDT [54]	≠0	0.6997	0.5925	0.5845	1.4945	0.5624	14.969
	HSDT [55]	0	0.7308	0.5806	0.5913	1.4874	0.5648	14.944
	HSDT [55]	≠0	0.702	0.5911	0.5868	1.4917	0.5647	14.945
	TSDT [10]		0.7284	0.5796	0.5889	1.4856	0.5625	14.9255
	SSDT [21]		0.728	0.5787	0.5889	1.4852	0.5625	14.9255
	HSDT [20]		0.7271	0.5779	0.5888	1.4849	0.5625	14.9255
	FiSDT[48]		0.725	0.5765	0.5885	1.4844	0.5625	14.9254
	Model 1		0.7254	0.5779	0.5885	1.4849	0.5625	14.9255
	Model 2		0.7204	0.5793	0.5878	1.4854	0.5625	14.9255
	Ref. [58]	≠0	1.1585	0.4877	0.8821	1.1971	0.8286	11.923
	CLT	0	0.8281	0.642	0.8281	1.6049	0.8281	16.049
	FSDT	0	1.1125	0.642	0.8736	1.6049	0.828	16.049
	GSDT [52]	0	-	-	0.8651	1.1783	-	-
	Ref. [53]	0	1.1673	0.5986	0.8828	1.5874	0.8286	16.047
	Ref. [53]	≠0	1.1585	0.4877	0.8821	1.1971	0.8286	11.923
	SSDT [54]	≠0	1.1178	0.4404	0.875	1.1783	0.8286	11.932
4	HSDT [55]	0	1.1553	0.4338	0.877	1.1592	0.8241	11.737
	HSDT [55]	≠0	1.1108	0.433	0.87	1.1588	0.824	11.737
	TSDT [10]		1.1599	0.4433	0.8815	1.1753	0.8287	11.8796
	SSDT [21]		1.1619	0.4408	0.8819	1.1742	0.8287	11.8796
	HSDT [20]		1.1627	0.4385	0.8821	1.1733	0.8287	11.8796
	FiSDT[48]		1.1614	0.4349	0.8819	1.1718	0.8287	11.8792
	Model 1		1.162	0.4371	0.882	1.1727	0.8287	11.8793
	Model 2		1.1562	0.4369	0.8812	1.1726	0.8287	11.8793
	Ref. [58]	≠0	1.3745	0.3695	1.0072	0.8965	0.9361	8.9077
	CLT	0	0.9354	0.4796	0.9354	1.199	0.9354	11.99
	FSDT	0	1.3178	0.4796	0.9966	1.199	0.936	11.99
	GSDT [52]	0	-	-	1.0089	0.8775	-	-
	Ref. [53]	0	1.3925	0.4345	1.009	1.1807	0.9361	11.989
	Ref. [53]	≠0	1.3745	0.1478	1.0072	0.8965	0.9361	8.9077
	SSDT [54]	≠0	1.349	0.3227	0.875	1.1783	0.8286	11.932
10	HSDT [55]	0	1.376	0.3112	0.9952	0.8468	0.9228	8.6011
	HSDT [55]	≠0	1.3334	0.3097	0.9888	0.8462	0.9227	8.601
	TSDT [10]		1.3908	0.3249	1.0087	0.876	0.9362	8.8804
	SSDT [21]		1.3917	0.3225	1.0089	0.875	0.9362	8.8804
	HSDT[20]		1.3906	0.3203	1.0088	0.8741	0.9362	8.8804
	FiSDT[48]		1.3862	0.317	1.0083	0.8727	0.9362	8.8801
	Model 1		1.3871	0.3189	1.0084	0.8735	0.9362	8.8802
	Model 2		1.3738	0.3183	1.0064	0.8732	0.9362	8.8802

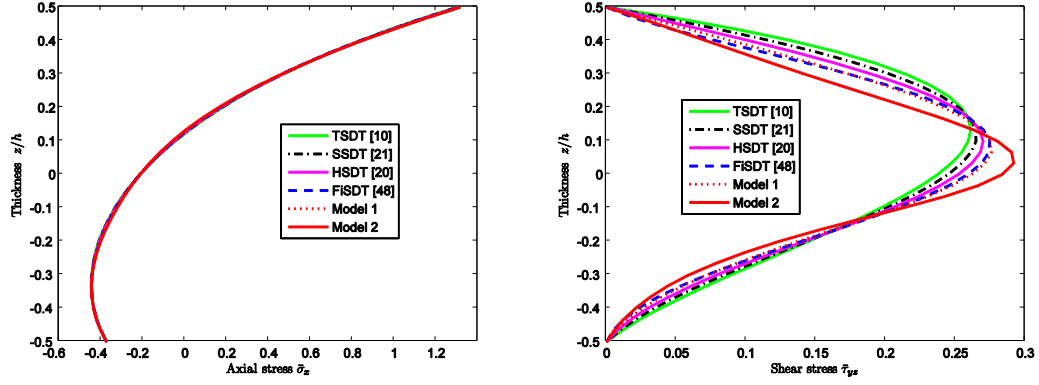


Figure 7. The stresses through thickness of Al/Al<sub>2</sub>O<sub>3</sub> FG plate under sinusoidal load with  $a/h=4$ ,  $n=1$ , via different refined plate models.

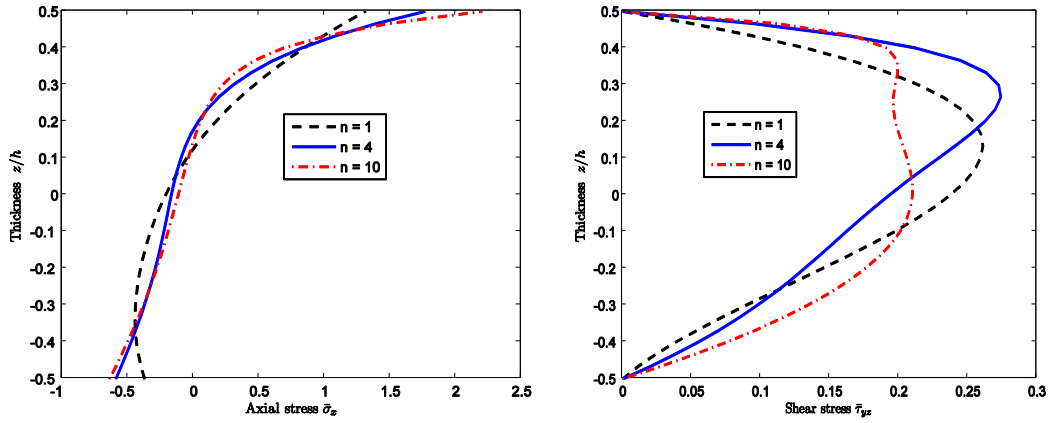


Figure 8. The stresses through thickness of Al/Al<sub>2</sub>O<sub>3</sub> FG plate under sinusoidal load with  $a/h=4$ ,  $n=1$  via various power indices  $n$ .

Figure 8 presents the curved distribution of the axial and shear stresses through the plate thickness according to power index  $n = 1, 4, 10$ , respectively. It can be concluded that the present model based on NURBS approximation yields very promising results compared to that given in Ref. [55].

Table 4: The non-dimension deflection of Al/ZrO<sub>2</sub>-1 plate under uniform load with  $a/h=5$  via different boundary conditions.

BC	$n$	Model				
		HOSNDPT[59]	TSDT[29]	PRT		
				FiSDT[48]	Model 1	Model 2
ceramic		0.5019	0.5088	0.5073	0.5074	0.506
	0.5	0.7543	0.7607	0.7587	0.7588	0.7568
	1	0.8708	0.8776	0.8754	0.8756	0.8732
SFSF	2	0.9744	0.9830	0.9808	0.981	0.9784



	4	-	1.0701	1.0676	1.0679	1.0648
	8	-	1.1577	1.1540	1.1544	1.1504
	metal	1.4345	1.4537	1.4490	1.4498	1.4458
	ceramic	0.1671	0.1716	0.1711	0.1711	0.1703
	0.5	0.2505	0.2554	0.2547	0.2548	0.2536
	1	0.2905	0.2955	0.2947	0.2948	0.2934
SSSS	2	0.328	0.3334	0.3327	0.3328	0.3312
	4	-	0.3655	0.3647	0.3649	0.363
	8	-	0.3958	0.3943	0.3945	0.3922
	metal	0.4775	0.4903	0.4887	0.4889	0.4865
	ceramic	0.0731	0.0734	0.0709	0.071	0.0701
	0.5	0.1073	0.1077	0.1041	0.1043	0.1029
	1	0.1253	0.1256	0.1215	0.1217	0.1201
CCCC	2	0.1444	0.1447	0.1401	0.1402	0.1384
	4	-	0.1622	0.1566	0.1568	0.1546
	8	-	0.1760	0.1694	0.1696	0.1669
	metal	0.2088	0.2098	0.2027	0.203	0.2001

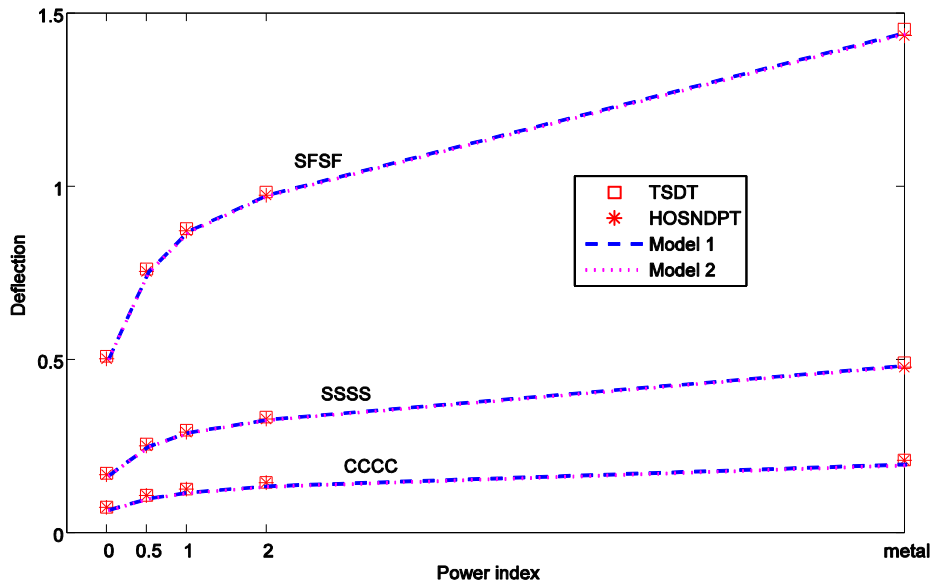


Figure 9. The normalized deflection of Al/ZrO<sub>2</sub>-1 FGM plate via power indexes and boundary conditions.

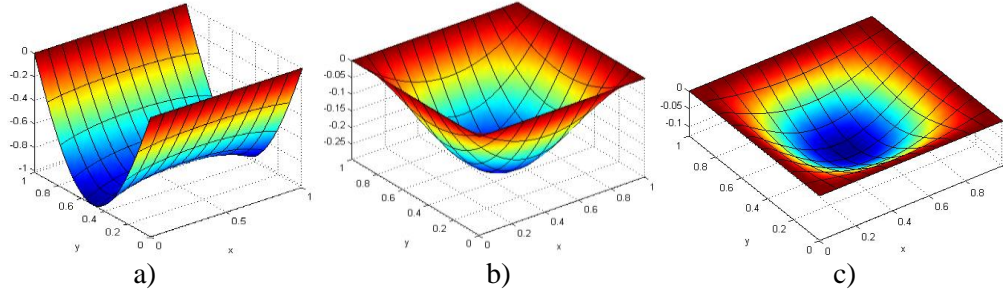


Figure 10. Deflection profile of Al/ZrO<sub>2</sub>-1 FGM plates: (a) SFSF; (b) SSSS; (c) CCCC.

To end this sub-section, the effective of boundary conditions on the normalized central deflection  $\bar{w}_c = 100w_c E_m h^3 / \{12(1-\nu^2)q_0 a^4\}$  of Al/ZrO<sub>2</sub>-1 plate is investigated. In this problem the Mori-Tanaka scheme is used for homogenizing Al/ZrO<sub>2</sub>-1 FGM plate. The present results listed in Table 4 are compared with those of Gilhooley[59] based on HOSNDPT using 18DOFs/node and Tran *et al.* [29] based on TSDT using 5 DOFs/node. Figure 9 shows that, by just using 4 DOFs/node, the present model produces solutions very close to Refs. [29,59] for all boundary conditions. Moreover, when the boundary condition changes from CCCC to SSSS and SFSF, the structural stiffness reduces, the magnitudes of deflection thus increase, respectively. The shapes of transverse displacement according the various boundary conditions are illustrated in Figure 10.

#### 4.3 Free vibration analysis

Let us consider a simply supported Al/ZrO<sub>2</sub>-1 plate which is homogenized by the Mori-Tanaka scheme. In Table 5, we also provide the results based on the RPT with various functions  $f(z)$  in [10, 48] and two current models 1 & 2 in comparison with the exact solution [50], that of HOSNDPT [47] and quasi 3D-solution using SSDT and HSDT [54, 55]. The excellent correlation between these models is again achieved for all values of exponent  $n$ . In addition, it is revealed that the proposed model 2 gives the best natural frequency with the least error compared to exact result [50] by Vel and Batra. The first ten natural frequencies of the thick and moderate plate with  $a/h = 5, 10, 20$  are listed in Table 6. The computed values agree well with the literature [47] for various  $a/h$  ratios and mode number. Corresponding to  $n = 1$ , the first six mode shapes are plotted in Figure 11.

Table 5: The natural frequency  $\bar{\omega} = \omega h \sqrt{\rho_m / E_m}$  of SSSS Al/ZrO<sub>2</sub>-1 plate with  $a/h=5$ .

Model	$\varepsilon_z$	$n$						
		0	0.5	1	2	3	5	10
Exact [50]	-	-	-	0.2192	0.2197	0.2211	0.2225	-
HOSNDPT [47]	-	-	-	0.2152	0.2153	0.2172	0.2194	-
				(-1.82)*	(-2.00)	(-1.76)	(-1.39)	

SSDT [54]	0	-	-	0.2184 (-0.36)	0.2189 (-0.36)	0.2202 (-0.41)	0.2215 (-0.45)	-
SSDT [54]	≠0	-	-	0.2193 (0.05)	0.2198 (0.05)	0.2212 (0.05)	0.2225 (0.00)	-
HSDT [55]	0	0.2459	0.2219	0.2184 (-0.36)	0.2191 (-0.27)	0.2206 (-0.23)	0.222 (-0.22)	0.2219
HSDT [55]	≠0	0.2469	0.2228	0.2193 (0.05)	0.22 (0.14)	0.2215 (0.18)	0.223 (0.22)	0.2229
	TSDT[10]	0.2459	0.2221	0.2184 (-0.36)	0.2189 (-0.36)	0.2203 (-0.36)	0.2216 (-0.40)	0.2211
	FiSDT[48]	0.2462	0.2224	0.2187 (-0.23)	0.2191 (-0.27)	0.2205 (-0.27)	0.2218 (-0.31)	0.2215
RPT	Model 1	0.2462	0.2224	0.2186 (-0.27)	0.2191 (-0.27)	0.2205 (-0.27)	0.2218 (-0.31)	0.2215
	Model 2	0.2468	0.2229	0.2192 (0.00)	0.2196 (-0.05)	0.221 (-0.05)	0.2224 (-0.04)	0.2222

(\*) The error in parentheses

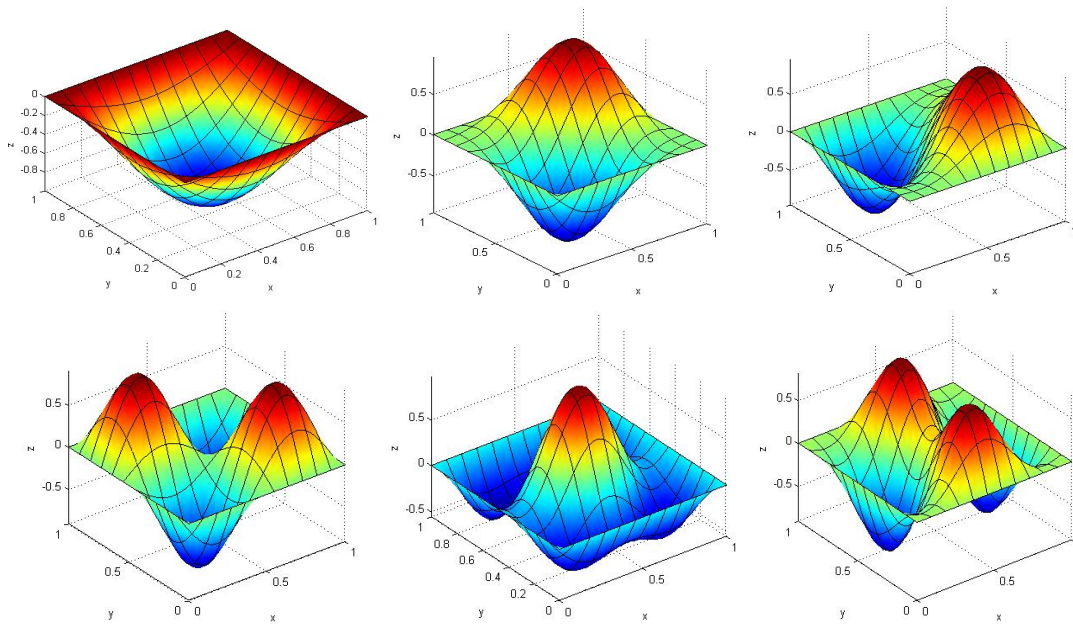


Figure 11 The first six mode shapes of Al/ZrO<sub>2</sub>-1 with  $n=1$ ,  $a/h=5$ .

Table 6: The natural frequency  $\bar{\omega}$  of SSSS Al/ZrO<sub>2</sub>-1 plate with various ratios  $a/h$ .

$a/h$	Model	Modes									
		1	(2,3)	4	5	6	7	8	9	10	
5	Exact [50]	0.2192	-	-	-	-	-	-	-	-	
	HOSNDPT [47]	0.2152	0.4114	0.4761	0.4761	0.582	0.6914	0.8192	0.8217	0.8242	
	FiSDT[48]	0.2187	0.4116	0.4806	0.4806	0.5821	0.6976	0.8233	0.8233	0.8263	
	RPT Model 1	0.2186	0.4116	0.4804	0.4804	0.5821	0.6972	0.8233	0.8233	0.8257	

	Model 2	0.2192	0.4116	0.4827	0.4827	0.5821	0.7018	0.8233	0.8233	0.832
10	Exact [50]	0.0596	-	-	-	-	-	-	-	-
	HOSNDPT [47]	0.0584	0.141	0.2058	0.2058	0.2164	0.2646	0.2677	0.2913	0.3264
	SSDT [54]	0.0596	0.1426	0.2058	0.2058	0.2193	0.2676	0.2676	0.291	0.3363
	HSDT [55]	0.0596	0.1426	0.2059	0.2059	0.2193	0.2676	0.2676	0.2912	0.3364
	FiSDT[48]	0.0595	0.1423	0.2058	0.2058	0.2187	0.2668	0.2668	0.2911	0.3351
	RPT Model 1	0.0595	0.1423	0.2058	0.2058	0.2187	0.2667	0.2667	0.2911	0.335
	Model 2	0.0596	0.1425	0.2058	0.2058	0.2192	0.2675	0.2675	0.2911	0.3362
20	Exact [28]	0.0153	-	-	-	-	-	-	-	-
	HOSNDPT [47]	0.0149	0.0377	0.0593	0.0747	0.0747	0.0769	0.0912	0.0913	0.1029
	SSDT [54]	0.0153	0.0377	0.0596	0.0739	0.0739	0.095	0.095	0.1029	0.1029
	HSDT [55]	0.0153	0.0377	0.0596	0.0739	0.0739	0.095	0.095	0.103	0.103
	FiSDT[48]	0.0153	0.0377	0.0595	0.0739	0.0739	0.0949	0.0949	0.1029	0.1029
	RPT Model 1	0.0153	0.0377	0.0595	0.0739	0.0739	0.0949	0.0949	0.1029	0.1029
	Model 2	0.0153	0.0377	0.0596	0.0739	0.0739	0.095	0.095	0.1029	0.1029

#### 4.4 Buckling analysis

In this section, a clamped circular plate of radius  $R$  and thickness  $h$  is subjected to a uniform radial pressure  $p_0$  is meshed into 11x11 cubic elements as shown in Figure 12. The plate made from Al/ZrO<sub>2</sub>-2 is homogenized following the rule of mixture, in which the effective Young's modulus  $E_e$  and Poisson's ratio  $\nu_e$  are calculated according to Eq. (35).

$$P_e = P_c V_c(z) + P_m V_m(z) \text{ where } V_m(z) = \left( \frac{1}{2} - \frac{z}{h} \right)^n, V_c = 1 - V_m \quad (35)$$

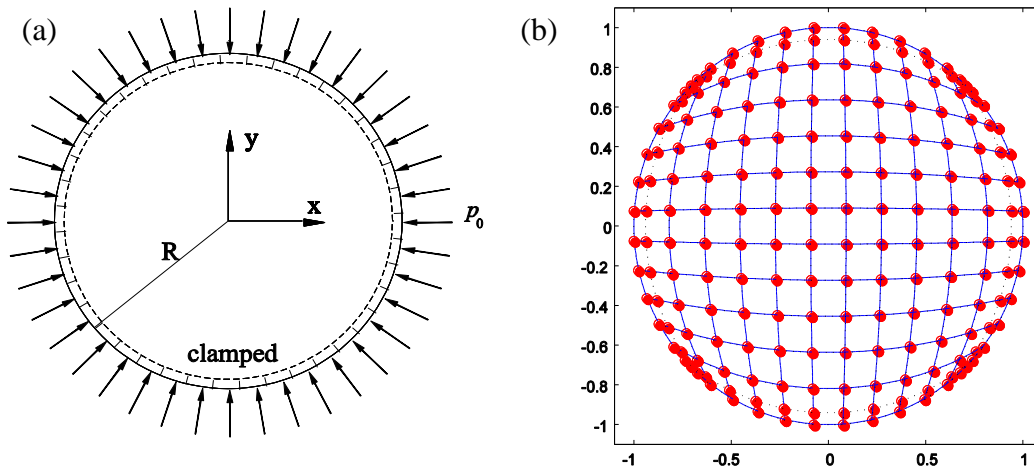


Figure 12. The circular plate: (a) geometry and (b) meshing of 11x11 cubic elements.

The variation of the critical load parameter  $\bar{p}_{cr} = p_{cr} R^2 / D_m$  versus the exponential value and the thickness to radius ratio is illustrated in Figure 13 and Figure 14 respectively. It is observed that the critical buckling load increases corresponding to the decrease in the  $h/R$  ratios and the increase in the value of  $n$ . When  $n > 10$ , it is slightly independent on the increment of the exponent  $n$ . Table 7 shows the comparison between present results with analytical solution published in the literatures [56,57] and numerical solution based on IGA [29] using TSDT. The RPT gives slightly higher values than TSDT [57,29] and unconstrained third-order shear deformation plate theory (UTSDT) [56] with the difference of 0.5% and 1.8%. However, the discrepancy between them reduces as plate becomes thinner. Figure 15 presents the first four buckling mode shapes of the clamped circular Al/ZrO<sub>2</sub>-2 plate with  $h/R = 0.1$  and  $n = 2$ .

Table 7: Comparison of the buckling load parameter of clamped thick circular Al/ZrO<sub>2</sub>-2 plate.

Power index	Method	$h/R$			
		0.1	0.2	0.25	0.3
0	FST [56]	14.089	12.571	11.631	10.657
	TST [57]	14.089	12.574	11.638	10.67
	UTSDT[56]	14.089	12.575	11.639	10.67
	TSDT[29]	14.1089	12.5914	11.6540	10.6842
	RPT FiSDT[48]	14.1873	12.6787	11.7466	10.7822
	Model 1	14.1859	12.6743	11.7405	10.7745
	Model 2	14.2023	12.7281	11.8143	10.8666
0.5	FST[56]	19.423	17.34	16.048	14.711
	TST[57]	19.411	17.311	16.013	14.672
	UTSDT[56]	19.413	17.31	16.012	14.672
	TSDT[29]	19.4391	17.3327	16.0334	14.6910
	FiSDT[48]	19.5458	17.4504	16.1579	14.8227
	RPT Model 1	19.5439	17.4441	16.1492	14.8118
	Model 2	19.5663	17.518	16.2506	14.9381
2	FST[56]	23.057	20.742	19.29	17.77
	TST[57]	23.074	20.803	19.377	17.882
	UTSDT[56]	23.075	20.805	19.378	17.881
	IGA-TSDT[29]	23.1062	20.8319	19.4033	17.9060
	FiSDT[48]	23.2361	20.9794	19.5612	18.0745
	RPT Model 1	23.2342	20.9728	19.552	18.0628
	Model 2	23.2592	21.0569	19.6687	18.2099
5	FST[56]	25.411	22.876	21.282	19.611
	TST[57]	25.439	22.971	21.414	19.78
	UTSDT[56]	25.442	22.969	21.412	19.778
	IGA-TSDT[29]	25.4743	22.99918	21.4407	19.80426
	FiSDT[48]	25.6172	23.1598	21.6118	19.9861
	RPT Model 1	25.6152	23.1529	21.6022	19.9738
	Model 2	25.6418	23.2426	21.7268	20.1313

	FST[56]	27.111	24.353	22.627	20.823
	TST[57]	27.133	24.423	22.725	20.948
	UTSDT[56]	27.131	24.422	22.725	20.949
10	TSDT[29]	27.1684	24.4542	22.7536	20.9750
	FiSDT[48]	27.3176	24.6148	22.9216	21.1509
PRT	Model 1	27.3155	24.6077	22.9117	21.1383
	Model 2	27.3429	24.6994	23.0389	21.2986

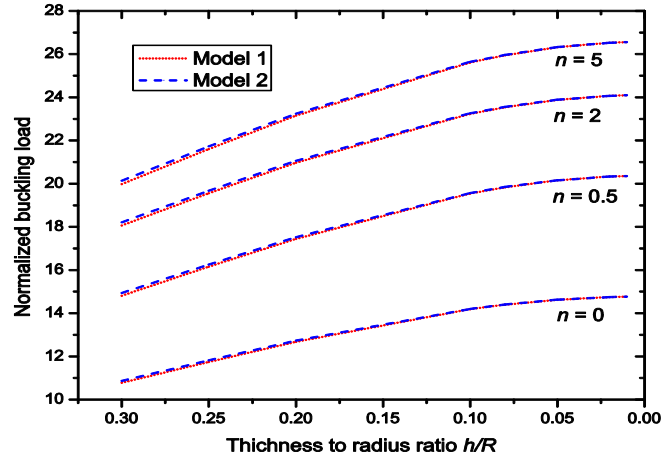


Figure 13. The normalized buckling load  $\bar{p}_{cr}$  of the Al/ZrO<sub>2</sub>-2 plate via radius to thickness ratio  $R/h$ .

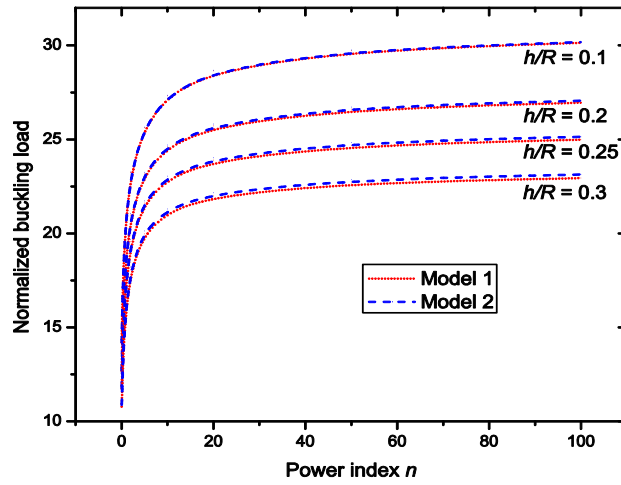


Figure 14. The normalized buckling load  $\bar{p}_{cr}$  of the Al/ZrO<sub>2</sub>-2 plate via power index  $n$ .

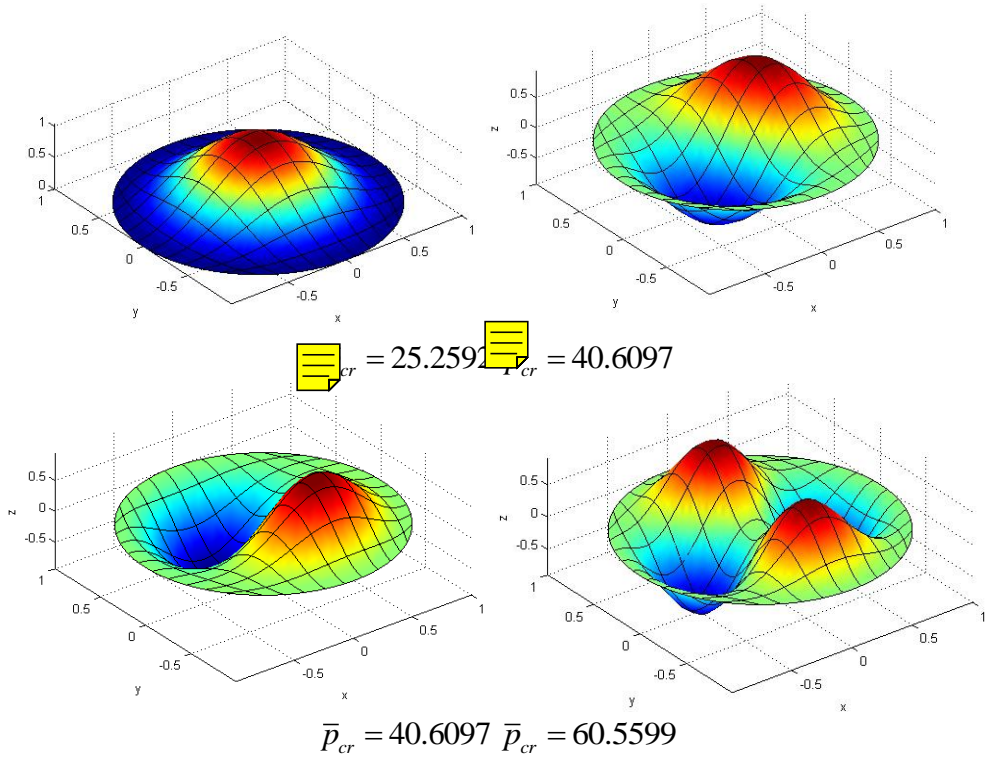


Figure 15. The first four buckling modes of Al/ZrO<sub>2</sub>-2 plate with  $h/R = 0.1$  and  $n = 2$ .

## 5. Conclusions

In this paper, we have developed the inverse tangent transverse shear deformation model together with the isogeometric finite element formulation for static, free vibration and buckling analyses of FGM plates. The method fulfills the  $C^1$  – requirement of RPT model and the approximate displacements have four DOFs per each control point which results in less computational cost compared to other five DOFs methods. In the present model, the shear strains/stresses are obtained independently on the bending component. As a result, RPT has been strongly similar to CPT and it naturally overcomes the shear locking phenomenon. The present results are compared with analytical solutions and those using HSDT or quasi-3D models and they demonstrated excellent agreement in static, free vibration and buckling problems. The present models ensured the non-linear distribution of the shear stress/strain through the plate thickness without using any shear correction factors, and yielded the traction-free boundary conditions at plate surfaces. Finally, it can be concluded that the proposed model 2 produces the high accuracy for analysis of FGM plates.

## References

1. Reissner E (1945) The effect of transverse shear deformation on the bending of elastic plates. *J Appl Mech Trans ASME* 12(2):69–77.
2. Mindlin RD (1951) Influence of rotary inertia and shear on flexural motions of isotropic, elastic plates *J Appl Mech Trans ASME* 18(1):31–38.
3. Young W. Kwon, Hyochoong Bang (2000) *The Finite Element Method Using MATLAB*, CRC Press; 2 edition.
4. Bathe KJ, Dvorkin EN (1985) A four-node plate bending element based on Mindlin–Reissener plate theory and a mixed interpolation. *Int J Numer Methods Eng* 21:367–383.
5. Tessler A, Hughes TJR (1985) A three-node Mindlin plate element with improved transverse shear. *Comput Methods Appl Mech Eng* 50:71–101.
6. Bletzinger KU, Bischoff M, Ramm E (2000) A unified approach for shear-locking free triangular and rectangular shell finite elements. *Comput Struct* 75:321–334.
7. Nguyen-Xuan H, Tran V. Loc, Nguyen-Thoi T, Vu-Do HC (2011) Analysis of functionally graded plates using an edge-based smoothed finite element method. *Compos Struct* 93: 3019–3039.
8. Nguyen-Xuan H, Tran V. Loc, Thai H. Chien, Nguyen-Thoi T (2012) Analysis of functionally graded plates by an efficient finite element method with node-based strain smoothing. *Thin-Walled Struct* 54:1–18.
9. Ferreira AJM, Castro LMS and Bertoluzza S (2003) A high order collocation method for the static and vibration analysis of composite plates using a first-order theory. *Compos Struct* 34(7):627–636.
10. Reddy JN (2000) Analysis of functionally graded plates. *Int J Numer Methods Eng* 47:663–684.
11. Ambartsumian SA (1958) On the theory of bending plates. *Izv Otd Tech Nauk ANSSSR* 5:269–277.
12. Reissner E (1975) On transverse bending of plates including the effects of transverse shear deformation. *IntJ Solids and Structures* 25:495–502.
13. Levinson M (1980) An accurate simple theory of statics and dynamics of elastic plates. *Mechanics Research Communications* 7:343–350.
14. Reddy JN (1984) A simple higher-order theory for laminated composite plates. *Journal of Applied Mechanics* 51:745–752.



15. Mantari JL, Oktem AS, Guedes Soares C (2012) Bending response of functionally graded plates by using a new higher order shear deformation theory, *Composite Structures* 94:714–723.
16. Zenkour AM (2009) The refined sinusoidal theory for FGM plates on elastic foundations *Int J Mech Sci* 51(11–12) 869–880.
17. Ait Atmane H, Tounsi A, Mechab I, Adda Bedia EA (2010) Free vibration analysis of functionally graded plates resting on Winkler-Pasternak elastic foundations using a new shear deformation theory. *Int J Mech Mater Des*6(2):113–121.
18. Soldatos KP (1992) A transverse shear deformation theory for homogenous monoclinic plates. *Acta Mechanica* 94:195–220.
19. Touratier M (1991) An efficient standard plate theory. *Int J Eng Sci* 29(8):901–916.
20. Karama M, Afaq KS, and Mistou S (2003) Mechanical behavior of laminated composite beam by new multi-layered laminated composite structures model with transverse shear stress continuity. *Int J Solids and Structures* 40:1525-1546.
21. Arya H, Shimpi RP, and Naik NK (2002) A zigzag model for laminated composite beams. *Composite Structures* 56(1):21-24.
22. Aydogdu M (2009) A new shear deformation theory for laminated composite plates. *Composite Structures* 89(1):94-101.
23. Thai HT, Choi DH (2011) A refined plate theory for functionally graded plates resting on elastic foundation. *Composites Science and Technology* 71(16):1850-1858.
24. Kim SE, Thai HT, Lee J (2009) A two variable refined plate theory for laminated composite plates. *Composite Structures* 89(2):197-205.
25. Shimpi RP (2002) Refined plate theory and its variants. *AIAA Journal* 40(1):137-146.
26. Shimpi RP, Patel HG (2006) A two variable refined plate theory for orthotropic plate analysis, *Int J Solids and Structures*, 43(22–23); 6783-6799.
27. Shimpi RP, Patel HG (2006) Free vibrations of plate using two variable refined plate theory, *J Sound Vib* 296(4–5): 979-999.
28. Thai H. Chien, Nguyen-Xuan H, Bordas SPA, Nguyen-Thanh N, Rabczuk T (2012) Isogeometric analysis of laminated composite plates using the higher-order shear deformation theory. *Mechanics of Advanced Materials and Structures*, (in press).
29. Tran V. Loc, Ferreira AJM, Nguyen-Xuan H (2013) Isogeometric analysis of functionally graded plates using higher-order shear deformation theory, *Composites Part B: Engineering* 51: 368-383.

30. Thai H. Chien, Tran V. Loc, Tran T. Dung, Nguyen-Thoi T, Nguyen-Xuan H (2012) Analysis of laminated composite plates using higher-order shear deformation plate theory and node-based smoothed discrete shear gap method, *Applied Mathematical Modelling*, 36:5657-5677.
31. Tran V. Loc, Nguyen-Thoi T, Thai H. Chien, Nguyen-Xuan H (2012) An edge-based smoothed discrete shear gap method (ES-DSG) using the  $C^0$ -type higher-order shear deformation theory for analysis of laminated composite plates, *Mechanics of Advanced Materials and Structures*, (in press).
32. Phung-Van P, Nguyen-Thoi T, Tran V. Loc, Nguyen-Xuan H (2013) A cell-based smoothed discrete shear gap method (CS-DSG3) based on the  $C^0$ -type higher-order shear deformation theory for static and free vibration analyses of functionally graded plates. *Computational Materials Science*, (in press).
33. Sankara CA and Igengar NGR (1996) A  $C^0$  element for free vibration analysis of laminated composite plates *J. Sound and Vib* 191:721–738.
34. Kant T, Swaminathan K (2002) Analytical solutions for the static analysis of laminated composite and sandwich plates based on a higher order refined theory, *Composite Structures*, 56(4); 329-344.
35. Reddy JN (1997) *Mechanics of laminated composite plates-theory and analysis*. New York: CRC Press.
36. Hughes TJR, Cottrell JA, and Bazilevs Y (2005) Isogeometric analysis: CAD, finite elements, NURBS, exact geometry and mesh refinement. *Comput Methods Appl Mech Eng* 194(39-41):4135–4195.
37. Cottrell JA, Hughes TJR, Bazilevs Y (2009) *Isogeometric Analysis, Towards Integration of CAD and FEA*, Wiley.
38. Elguedj T, Bazilevs Y, Calo V, and Hughes T (2008) B and F projection methods for nearly incompressible linear and non-linear elasticity and plasticity using higher-order NURBS elements. *Comput Methods Appl Mech Eng* 197:2732-2762.
39. Cottrell JA, Reali A, Bazilevs Y, and Hughes TJR (2006) Isogeometric analysis of structural vibrations. *Comput Methods Appl Mech Eng* 195(41-43):5257–5296.
40. Benson DJ, Bazilevs Y, Hsu MC, and Hughes TJR Isogeometric shell analysis: The Reissner–Mindlin shell. *Comput Methods Appl Mech Eng* 199(5-8): 276–289.
41. Kiendl J and Bletzinger KU, Linhard J, and Wchnner R (2009) Isogeometric shell analysis with Kirchhoff-Love elements, *Comput Methods Appl Mech Eng* 198(49-52):3902–3914.

42. Wall WA, Frenzel MA, and Cyron C (2008) Isogeometric structural shape optimization. *Comput Methods Appl Mech Eng* 197(33-40): 2976–2988.
43. Thai H. Chien, Nguyen-Xuan H, Nguyen-Thanh N, Le T-H, Nguyen-Thoi T (2012) Rabczuk T, Static, free vibration, and buckling analysis of laminated composite Reissner–Mindlin plates using NURBS-based isogeometric approach, *Int J Numer Meth Engng* 91(6):571–603.
44. Nguyen-Thanh N, Kiendl J, Nguyen-Xuan H, Wüchner R, Bletzinger KU, Bazilevs Y, Rabczuk T (2011) Rotation free isogeometric thin shell analysis using PHT-splines. *Comput Methods Appl Mech Eng* 200(47-48): 3410-3424.
45. Mori T, Tanaka K (1973) Average stress in matrix and average elastic energy of materials with misfitting inclusions. *Acta Metall* 21: 571–574.
46. Vel SS, Batra RC (2004) Exact solution for thermoelastic deformations of functionally graded thick rectangular plates, *AIAA Journal* 40 1021–1033.
47. L.F. Qian, R.C. Batra, L.M. Chen, Static and dynamic deformations of thick functionally graded elastic plate by using higher-order shear and normal deformable plate theory and meshless local Petrov–Galerkin method. *Composites Part B Engineering* 35 (6–8):685–97.
48. Nguyen-Xuan H, Thai H Chien, Nguyen-Thoi T (2013) Isogeometric finite element analysis of composite sandwich plates using a new higher order shear deformation theory, *Composite Part B* (in press), Doi: 10.1016/j.compositesb.2013.06.044.
49. Auricchio F, Beiraoda Veiga F, Buffa A, Lovadina C, Reali A, and Sangalli G (2007) A fully locking-free isogeometric approach for plane linear elasticity problems: a stream function formulation. *Comput Methods Appl Mech Eng* 197:160–172.
50. Vel SS and Batra RC (2004) Three-dimensional Exact Solution for the Vibration of Functionally Graded Rectangular Plates. *J Sound Vib* 272:703-730.
51. Timoshenko SP, Woinowsky-Krieger S (1970) *Theory of plate and shell*. 3rd edition McGraw-Hill, Publishing Company.
52. Zenkour AM (2006) Generalized shear deformation theory for bending analysis of functionally graded plates. *Applied Mathematical Modelling* 30(1):67-84.
53. Carrera E, Brischetto S, Cinefra M, Soave M (2011) Effects of thickness stretching in functionally graded plates and shells *Composites Part B: Engineering* 42(2):123-133.
54. Neves AMA, Ferreira AJM, Carrera E, Roque CMC, Cinefra M, Jorge RMN, Soares CMM (2012) A quasi-3D sinusoidal shear deformation theory for the static and free vibration analysis of functionally graded plates, *Composites Part B: Engineering* 43(2):711–725.

55. Neves AMA, Ferreira AJM, Carrera E, Cinefra M, Roque CMC, Jorge RMN, Soares CMM (2013) Static, free vibration and buckling analysis of isotropic and sandwich functionally graded plates using a quasi-3D higher-order shear deformation theory and a meshless technique, *Composites Part B: Engineering* 44(1):657-674.
56. Saidi AR , Rasouli A, Sahraee S (2009) Axisymmetric bending and buckling analysis of thick functionally graded circular plates using unconstrained third-order shear deformation plate theory, *Composite Structures* 89:110–119.
57. Ma LS, Wang TJ (2004) Relationship between axisymmetric bending and buckling solutions of FGM circular plates based on third-order plate theory and classical plate theory. *Int J Solids Struct* 41:85–101.
58. Carrera E, Brischetto S, Robaldo A (2008) Variable kinematic model for the analysis of functionally graded material plates, *AIAA Journal* 46(1):194-203.
59. Gilhooley DF, Batra RC, Xiao JR, McCarthy MA, Gillespie JW (2007) Analysis of thick functionally graded plates by using higher-order shear and normal deformable plate theory and MLPG method with radial basis functions. *Comput Struct* 80:539–552.